OPEN ACCESS
IOP Publishing
Nanotechnology

Nanotechnology **36** (2025) 135301 (6pp)
https://doi.org/10.1088/1361-6528/adad7d

The effect of Ga-ion irradiation on sub-micron-wavelength spin waves in yttrium-iron-garnet films

Johannes Greil[1,*], Martina Kiechle[1], Adam Papp[2], Peter Neumann[3], Zoltán Kovács[3], Janos Volk[3], Frank Schulz[4], Sebastian Wintz[5], Markus Weigand[5], György Csaba[2] and Markus Becherer[1]

[1] School of Computation, Information and Technology, Technical University of Munich, München, Germany
[2] Faculty of Information Technology and Bionics, Pázmány Péter Catholic University, Budapest, Hungary
[3] HUN-REN Center for Energy Research, Budapest, Hungary
[4] Max-Plank-Institut für Intelligente Systeme, Stuttgart, Germany
[5] Helmholtz-Zentrum Berlin (HZB), Berlin, Germany

E-mail: johannes.greil@tum.de

Received 26 August 2024, revised 14 January 2025
Accepted for publication 23 January 2025
Published 5 February 2025

Abstract

We investigate the effect of focused-ion-beam (FIB) irradiation on spin waves with sub-micron wavelengths in yttrium-iron-garnet films. Time-resolved scanning transmission x-ray microscopy was used to image the spin waves in irradiated regions and deduce corresponding changes in the magnetic parameters of the film. We find that the changes of Ga^+ irradiation can be understood by assuming a few percent change in the effective magnetization M_{eff} of the film due to a trade-off between changes in anisotropy and effective film thickness. Our results demonstrate that FIB irradiation can be used to locally alter the dispersion relation and the effective refractive index n_{eff} of the film, even for submicron wavelengths. To achieve the same change in n_{eff} for shorter wavelengths, a higher dose is required, but no significant deterioration of spin wave propagation length in the irradiated regions was observed, even at the highest applied doses.

Supplementary material for this article is available online

Keywords: magnonic devices, spin-wave applications, ion irradiation, thin films

* Author to whom any correspondence should be addressed.

1. Introduction

Magnonics has seen explosive development in recent years, with many technological breakthroughs [1–5] and interesting device concepts [6–9]. As the field matures, it becomes gradually more important to develop industry-standard fabrication technologies that are versatile, flexible, scalable, and widely accessible. Since the focus is drifting toward applications, the complexity of the devices in a single magnonic unit (i.e. a device block without internal electrical conversion) is increasing, requiring more sophisticated patterning technologies. Recently, focused-ion-beam (FIB) irradiation of yttrium-iron-garnet (YIG) has been demonstrated as a tool for fabricating optical elements for spin waves [10]. Instead of physically removing material to create patterns, this method introduces local changes in the crystal structure of YIG, effectively modifying the local dispersion properties of spin waves. In effect, gradient-index steering of spin waves becomes achievable for both classical optical geometries and inverse-designed scatterers with possible applications in the field of signal classification, spectral analysis, or spatial separation of signals in a fully analog way [10, 11]. This technique has a high resolution, limited mainly by the vertical and lateral straggle of the ions, which is typically less than the film thickness or a few tens of nanometers. In research labs, it provides a rapid prototyping workflow, as it does not require lithography or a clean room environment. Moreover, it can be applied multiple times successively to further adjust the device characteristics. With regard to mass production, ion-irradiation can be adapted to production lines using ion implanter technology combined with hard masks, which is a standard technology in modern CMOS production lines. Typical energy levels for implanter technology range from keV to MeV, which covers a wider range than most research-grade FIB tools [12]. The local film modification is stable over time, as ion diffusion and changes in the crystal structure of the sample do not occur at moderate temperatures, although elevated temperatures (e.g. subsequent annealing of the sample) can induce changes in the crystal structure and reverse the effects of FIB irradiation.

In this work, we were interested in finding out the trade-offs of using the technology of Ga^+-ion irradiation for spin waves with an order of magnitude smaller wavelengths, i.e. a few hundred nanometers instead of a few microns as demonstrated in [10]. For this purpose, we carried out time-resolved scanning transmission x-ray microscopy (TR-STXM) at the Maxymus end station [13] of the BESSY II electron storage ring, operated by the Helmholtz–Zentrum Berlin für Materialien und Energie on samples with sub-micron stripline transducers to excite spin waves. We measured wavelengths down to 700 nm for a lateral map of several ion doses. We obtained an assessment of the required doses for sub-micron wavelengths where even relatively high doses do not significantly deteriorate spin wave propagation lengths.

2. Methods

In our experiment, we used a YIG film of 100 nm thickness purchased from Innovent Jena. The film was grown by means of liquid phase epitaxy on a GGG substrate [14], with an extracted intrinsic effective magnetization M_{eff} of 133 kA m^{-1}. For thinning the GGG substrate to a membrane thickness of several hundred nanometers in an area of 135 μm by 95 μm, mechanical polishing in combination with Ga^+ FIB milling, similar to the process described in [15] was used. The optical microscope image in figure 1(a) shows the sample geometry. The upper stripline transducer is bond-wired to the sample carrier and supplied by a radio-frequency signal source to excite spin waves, while the lower transducer is unconnected/unsupplied and not used for excitation. The stripline transducers with a width of 500 nm were fabricated using electron-beam lithography, thermal evaporation of a Cr(8 nm)/Cu(180 nm)/Cr(8 nm) stack, and lift-off processing. The backside-thinned YIG/GGG membrane shows thin-film interference for optical wavelengths, indicating a slight thickness variation of the overall membrane across the prepared window, which thus appears to be rainbow-colored. The brown nested rectangles around the membrane are thicker GGG remnants of the step-wise decreasing area in the backside etching process. The brightness change in the absolute STXM picture in figure 2(a) shows that the thickness of the YIG/GGG membrane has a negligible variation in the evaluated region [15].

For the Ga^+-ion irradiation of the YIG film, we used a 50 kV Micrion 9500 EX FIB tool. The mean penetration depth of the accelerated Ga^+-ions at 50 kV is about 25 nm according to SRIM simulations [16] and the TEM measurements presented in the supplementals of [10].

To achieve maximum x-ray magnetic circular dichroism (XMCD) contrast, the presented measurements were conducted at the central Fe L_3 XMCD peak of YIG at a nominal photon energy of 709.6 eV. The sample was mounted 30° tilted relative to the incident beam to gain sensitivity for forward volume (FV) spin waves, and magnetic fields were applied perpendicular to the sample plane in a range between −250 mT to 250 mT [17].

3. Results

We measured the wavelength of spin waves in the intrinsic YIG film and in irradiated regions at various bias fields in the FV configuration, i.e. with an out-of-plane bias field. Exemplary snapshots of the absolute and normalized (divided by the time average) STXM measurement are shown in figures 2(a) and (b) respectively, for a DC magnetic bias field of $B = 242.5$ mT. Spin wave propagation can be detected in the four dose fields, whereas the lower two fields show less signal amplitude because the waves must pass the intrinsic region between the transducers. Moreover, in figure 2(b), the

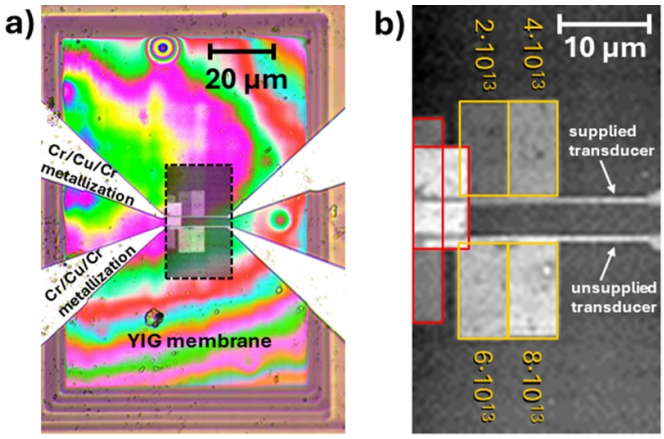

Figure 1. (a) Optical microscope image of the sample geometry. The superimposed black-white image shows the image from (b) for reference. (b) Normalized STXM image of the investigated sample area. Regions irradiated by FIB are indicated with the corresponding dose in ions cm^{-2} and a yellow frame. Regions indicated by a red frame were irradiated for alignment purposes, partially overlapping with the dose map.

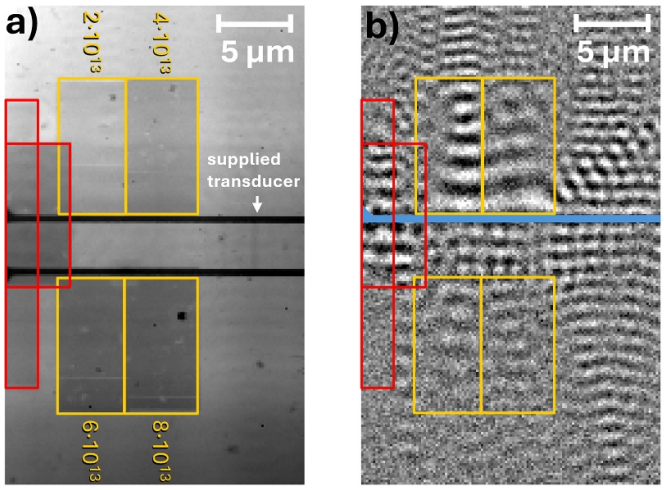

Figure 2. Recorded TR-STXM images of the spin-wave propagation for a bias field of $B = 242.5\,\mathrm{mT}$. A yellow frame indicates irradiated regions, and alignment regions with respect to the transducer are indicated by red frames. (a) A recoded snapshot image before subtracting the static background. Irradiated regions are visible as darker areas in the static, partially magnetic contrast, with higher doses resulting in darker shades. (b) Normalized TR-STXM snapshot, from the same experiment. The intensity in the lower boxes (higher doses) is typically smaller since the transducer does not excite waves directly in these regions. Intrinsic spin waves have to cover the distance to the unsupplied transducer (lower horizontal line in (a)) and cross the boundary of the irradiated regions. These waves are also partially reflected from the boundary.

transition between the upper dose fields and the intrinsic film is visible, showing the abrupt change in wavelength when irradiating areas with sharp borders. Throughout the measurements, we observed reflections on such boundaries at normal incidence and scattering, which is mainly visible in the intrinsic area right to the dose map in figure 2(b). Both were undesired effects but did not obscure the wavelength evaluation.

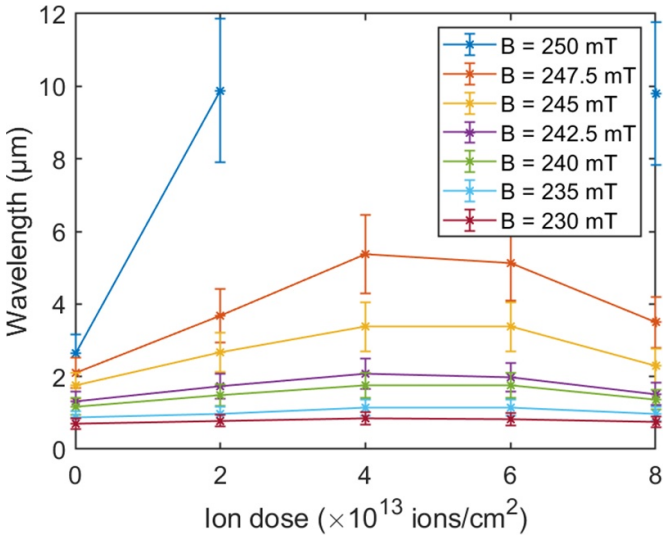

Figure 3. Measured spin wave wavelength vs. Ga^+-ion dose. The colored curves correspond to different applied bias fields, as indicated in the legend. The wavelength initially increases in all cases as a result of the irradiation, and the maximum change in wavelength occurs around 4×10^{13} ions cm^{-2}. For higher doses, the wavelength decreases again. Overall, the change in wavelength is smaller for shorter intrinsic wavelengths. Error bars represent the limited resolution of wavelength detection due to the finite irradiated box length.

The extracted wavelengths for the intrinsic and irradiated areas at different bias fields are plotted in figure 3. The frequency of the excitation was kept constant at $f = 2.57\,\mathrm{GHz}$. We observe a non-monotonic behavior as the wavelength first increases with the dose, but after a maximal change occurring between 4–6 $\times 10^{13}$ ions cm^{-2}, the trend reverses. This behavior was also observed in [10], but the wavelength in that case decreased initially and reached a local minimum. The two samples are similar in most parameters, except for the dose levels (one order of magnitude higher in the present study), the range of wavelengths excited (almost an order of magnitude lower in the present study), and the fact that the substrate was thinned down to a membrane for x-ray transparency. The latter aspect could change the effect of strain in the system, which may occur at a comparatively large area across the membrane, while the Ga^+-FIB backside milling is not affecting the YIG layer directly [15].

We have plotted the wavenumber for the different dose levels as a function of the bias field in figure 4. We fitted analytical curves to the data using the dispersion formulas developed by Kalinikos and Slavin [18, 19], which can be written in the FV configuration as

$$\omega^2 = \omega_H \left(\omega_H + \omega_M P\right), \tag{1}$$

where

$$P = 1 - \frac{1 - \mathrm{e}^{-kt_{\mathrm{eff}}}}{kt_{\mathrm{eff}}}, \tag{2}$$

$$\omega_H = \gamma \left(B_{\mathrm{ext}} - \mu_0 M_{\mathrm{eff}} + \frac{2A}{M_{\mathrm{eff}}} k^2\right), \tag{3}$$

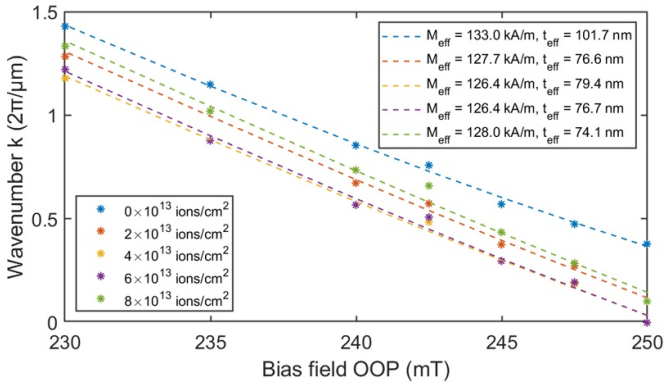

Figure 4. Measured dependency of the wavenumber on the bias field for the various applied dose levels. Dashed lines indicate analytical curves based on the Kalinikos and Slavin dispersion model with fitted effective magnetization and film thickness values indicated in the legend.

$$\omega_M = \gamma \mu_0 M_{\text{eff}}. \tag{4}$$

Here γ is the gyromagnetic ratio, μ_0 is the vacuum permittivity, A is the exchange stiffness, and B_{ext} is the external bias field applied out of plane. We fitted the analytical curves on the experimental data using effective magnetization M_{eff} and effective YIG film thickness t_{eff} as fitting parameters. These two can be uniquely extracted from the fit with good accuracy because t_{eff} has no influence on the FMR frequency ($k = 0$), while M_{eff} has a strong influence. The curves in figure 4 are close to linear. Thus, we can approximately think about a change in t_{eff} as a change of the slope (without sign reversal), while M_{eff} shifts the curve without significant change in the slope. All the other parameters (frequency, bias field, wavelength, etc) were well-controlled or measured in the experiment. Due to the almost symmetrical shape of the curves in figure 3, the fitted wavenumber curves in figure 4 coincidentally appear in pairs (i.e. 2×10^{13} ions cm^{-2} & 8×10^{13} ions cm^{-2} and 4×10^{13} ions cm^{-2} & 6×10^{13} ions cm^{-2} result in almost the same extracted values, respectively).

The fitted thicknesses (approximately 75 nm to 80 nm instead of the original 100 nm) are in line with the expected mean penetration depth of the Ga$^+$-ions at 50 keV acceleration voltage. TEM measurements show that approximately the top 25 nm of the crystal receives the most damage and gets amorphous [10]. The results suggest that in all the irradiated cases, the top 25 nm of the crystal is almost completely destroyed but not removed. Thus, the wavelength differences between the different dose levels are not primarily due to a physical thickness change in the film but due to a change in M_{eff} containing the contribution from a magnetoelastic field caused by the strain in the crystal. In addition to the effective magnetic thickness change, the effective magnetization M_{eff} was found to decrease by approximately 5 kA m^{-1} and 7 kA m^{-1} for the irradiated regions, as also indicated in the legend of figure 4. This is the opposite of the change identified in [10], where M_{eff} increased for lower doses up to a certain point and then decreased below the intrinsic value for higher doses. Since the top layer becomes almost entirely amorphous, and the bottom layer cannot be affected directly by the Ga$^+$-ions, we suggest that the effective magnetization change is due to a strain-induced anisotropy, also supported by previous studies on irradiated ferrites [20, 21]. The dose value for a turning point, as shown in figure 3, is specific to the acceleration voltage, the film composition and its intrinsic thickness, and the type of irradiated ions, which implicitly define the interplay between parameters like the mean penetration depth and the stopping/damaging effects in the crystal and their spread in thickness [22].

Using the XMCD contrast pictures of the dose map in figure 1(b), it is possible to estimate the change of effective crystalline YIG thickness in the irradiated fields relative to the intrinsic film. The transmitted light intensity I is calculated via the well-known Lambert–Beer law $I = I_0 \exp(-\sigma t)$, with the incident light intensity I_0, and the film thickness t. The material parameter $\sigma = \overline{\sigma} + \sigma_{\text{M}}$ splits up in a material-related contribution $\overline{\sigma}$ capturing effects like molar or density absorbance that is assumed approximately constant in our experiment, and a magnetic contribution σ_{M} that is proportional to the magnetization or spin polarization of the material (Fe in this case). Under the assumption that only t and σ_{M} may change due to irradiation, the relative change in magnetization and thickness (together: the total magnetic moment) due to irradiation with dose Dx can be estimated via

$$\frac{M_{\text{Dx}}}{M_0}\frac{t_{\text{Dx}}}{t_0} \propto \frac{\ln\left(I^+_{\text{Dx}}/I^-_{\text{Dx}}\right)}{\ln\left(I^+_0/I^-_0\right)}, \tag{5}$$

where $I^{\pm}_{\text{Dx}}$ is the measured light intensity for an external magnetic DC bias field of ± 250 mT, t_0 is the original YIG film thickness, and t_{Dx} is the effective magnetic crystalline YIG film thickness in the irradiated area with dose Dx. Note that from (5), it is not possible to differentiate between a change in magnetization and a change in thickness. However, we know from previous studies [10] and SRIM simulations that the Ga$^+$-ion penetration depth is approximately 25 nm, and there is no change in the physical thickness of the film since the ion etching is negligible at these dose levels. Additionally, the number of implanted Ga$^+$ ions is low compared to the Fe concentration such that the change due to variations, e.g. in the number density, molar absorptivity, or amount concentration represented by $\overline{\sigma}$ is negligible. Thus, ion irradiation does not directly affect the bottom 75 nm of the YIG film. The XMCD contrast change results from the decreasing saturation magnetization of the top irradiated layer. The change in total magnetic moment corresponding to an effective thickness of the YIG film that is proportional to the XMCD contrast change is plotted in figure 5 on the left ordinate. For the extraction, we additionally use the contrast of the alignment field, which was done at a dose of 12×10^{13} ions cm^{-2}. The extracted effective thickness shows good agreement with the TEM measurements in [10] and saturates close to the mean penetration depth of the Ga$^+$-ion at 75 nm. The fitted YIG thicknesses in figure 4, which denote the slope of the wavenumber curves, are additionally plotted on the left ordinate in figure 5, and

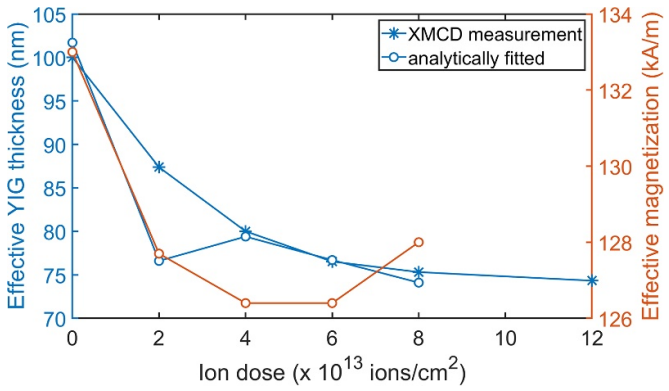

Figure 5. Left ordinate: the change of effective crystalline YIG thickness due to the Ga^+-ion irradiation based on the XMCD contrast picture in figure 1(b). For comparison, the fitted effective YIG thickness based on the analytical dispersion relations shown in figure 4 are plotted. The measured effective thickness saturates at around 75 nm, which coincides with the results in [10] and SRIM simulations. The dose of 12×10^{13} ions cm^{-2} in the alignment field was used in addition to the intended dose map. Right ordinate: extracted effective magnetization from the fitted dispersion relations in figure 4.

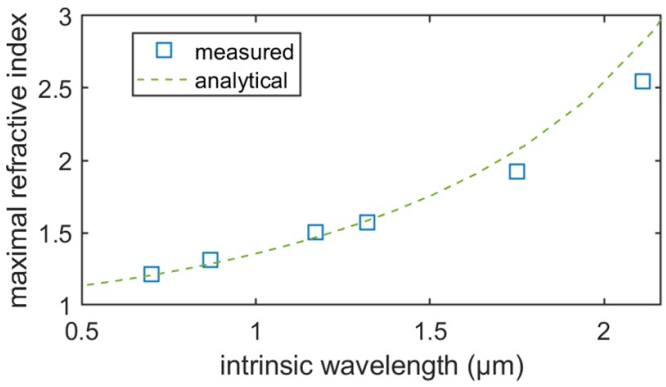

Figure 6. Maximum experimentally achievable refractive index, i.e. the change of wavelength in an irradiated area compared to the intrinsic wavelength, corresponding to the dose of 4×10^{13} ions cm^{-2}.

agree with the measured values. For comparison, we plot the extracted M_{eff} from the legend of figure 4 on the right ordinate of figure 5. As a result, we observe a trade-off between two effects: at low doses, implanted Ga^+-atoms locally induce strain in the YIG crystal as they generate a lattice displacement [20, 21]. This effect continues until a Ga concentration is reached, where the crystal is increasingly damaged and gets amorphous, which means that the effective thickness of the YIG film is reduced, and the strain-induced anisotropy gets partially compensated [22].

From the perspective of applications, it is instructive to plot the maximum achievable effective refractive index for spin waves against the intrinsic wavelength as shown in figure 6. The maximum change in our measurements occurred around 4×10^{13} ions cm^{-2}, so we plot the refractive indices for this dose value. Indeed we see the refractive index increase for larger wavelengths at the same dose value and the same M_{eff}. This tendency agrees well with the curve calculated from the analytical dispersion relation, plotted in figure 6 as a dashed line. The reason for this is that a small change in M_{eff} in the dispersion curves corresponds approximately to a shift along the wavenumber axis. This shift in k is approximately constant but decreases for larger wavenumbers if expressed as a fraction of k. More precisely, $n = \frac{k_0}{k} \approx \frac{k_0}{k_0 - \Delta k} \xrightarrow{k \to 0} 1$, where k_0 is the intrinsic wavenumber and Δk is the shift of the dispersion curves in k.

For a rough estimate, we can also state that the required dose for a given refractive index is inversely proportional to the intrinsic wavelength, not considering the nonlinearity of the dispersion relation. This can also be deduced from analytical considerations of the dispersion relation. More importantly, this study demonstrates that one order of magnitude higher dose (compared to [10]) does not hinder the propagation of spin waves. The attenuation of the waves in our measurements is only slightly affected, as can be seen in the normalized STXM snapshot of propagating spin waves in figure 2(b). Due to interference and diffraction effects in the experimental geometry, we were not able to extract quantitative damping values for the dose levels. We estimate that in the worst case, the propagation length is cut by half for the highest dose value, which is still very promising from an application point of view. At the same time, the higher (compared to [10]) refractive index allows for smaller lateral scatterer dimensions, which compensates partly for the reduced propagation and makes further downscaling of spin-wave devices with access to submicron wavelengths feasible. Reflection still occures at the boundaries between irradiated regions, with similar behavior as in optics, i.e. larger relative refraction index will result in higher reflection coefficients. To mitigate this effect, we suggest that the usual optical techniques could be utilized, e.g. smooth (graded index) transition between boundaries or antireflection layers. The range of practical refractive indices for optical designs including the corresponding dose levels, is limited, and the values presented in this work are sufficient for most applications.

4. Conclusion

We have measured the effect of Ga^+-ion irradiation on short-wavelength spin waves in thin YIG films. We observe a non-monotonic change in wavelength, which we attribute to a strain-induced anisotropy in the film in combination with an effective magnetic thickness change. The trade-off between the build-up of strain at lower doses and its release due to amorphization at higher doses could explain the turning point in measured wavelength shown in figure 3. We compared our experimental results with analytical calculations using the irradiation modeled as a change in effective magnetization and a decreased effective film thickness due to an amorphized top layer of YIG. We observe a decreased effect of irradiation for

smaller wavelengths, which the dispersion relation can directly explain.

Our results prove that graded-index FIB patterning can also be used for short-wavelength spin waves, while the required higher doses do not induce substantial losses to the spin wave propagation in the YIG medium. The nanoscale patterning of YIG is challenging, although several groups have developed methods to create YIG nanostructures due to their high relevance for magnonics. Nevertheless, the FIB irradiation technology's simplicity and ability to create graded-index nanoscale patterns are currently unparalleled among YIG patterning technologies for spin wave devices.

Data availability statement

All data that support the findings of this study are included within the article (and any supplementary files).

Acknowledgments

We thank Thomas Meisner, Ulrike Eigenthaler, and Marion Hagel (Max Planck Institute for Intelligent Systems, Stuttgart, Germany) for performing the mechanical thinning, FIB backside etching, and patterning of the transducers, respectively. The authors thank Helmholtz-Zentrum Berlin for the allocation of synchrotron radiation beamtime. A P acknowledges support from the Bolyai Janos Fellowship of the Hungarian Academy of Sciences.

ORCID iDs

Johannes Greil https://orcid.org/0009-0009-5693-7736
Zoltán Kovács https://orcid.org/0009-0005-8564-4132
Sebastian Wintz https://orcid.org/0000-0001-6138-8078

References

[1] Chumak A V *et al* 2022 Advances in magnetics roadmap on spin-wave computing *IEEE Trans. Magn.* **58** 1–72
[2] Zenbaa N *et al* 2024 Magnonic inverse-design processor (arXiv:2403.17724v1)
[3] Breitbach D *et al* 2023 Stimulated amplification of propagating spin waves *Phys. Rev. Lett.* **131** 156701
[4] Breitbach D *et al* 2024 Nonlinear erasing of propagating spin-wave pulses in thin-film Ga:YIG *Appl. Phys. Lett.* **124** 092405
[5] Merbouche H, Divinskiy B, Gouéré D, Lebrun R, El Kanj A, Cros V, Bortolotti P, Anane A, Demokritov S O and Demidov V E 2024 True amplification of spin waves in magnonic nano-waveguides *Nat. Commun.* **15** 1560
[6] Wang Q *et al* 2024 All-magnonic repeater based on bistability *Nat. Commun.* **15** 7577
[7] Wang Q, Csaba G, Verba R, Chumak A V and Pirro P 2024 Nanoscale magnonic networks *Phys. Rev. Appl.* **21** 040503
[8] Casulleras S, Knauer S, Wang Q, Romero-Isart O, Chumak A V and Gonzalez-Ballestero C 2023 Generation of spin-wave pulses by inverse design *Phys. Rev. Appl.* **19** 064085
[9] Flebus B *et al* 2024 The 2024 magnonics roadmap *J. Phys.: Condens. Matter* **36** 363501
[10] Kiechle M, Papp A, Mendisch S, Ahrens V, Golibrzuch M, Bernstein G H, Porod W, Csaba G and Becherer M 2023 Spin-wave optics in YIG realized by ion-beam irradiation *Small* **19** 2207293
[11] Kiechle M, Maucha L, Ahrens V, Dubs C, Porod W, Csaba G, Becherer M and Papp A 2022 Experimental demonstration of a spin-wave lens designed with machine learning *IEEE Magn. Lett.* **13** 1–5
[12] Nastasi M and Mayer J W 2006 *Ion Implantation and Synthesis of Materials* (Springer) (https://doi.org/10.1007/978-3-540-45298-0)
[13] Weigand M, Wintz S, Gräfe J, Noske M, Stoll H, Van Waeyenberge B and Schütz G 2022 TimeMaxyne: a shot-noise limited, time-resolved pump-and-probe acquisition system capable of 50 GHz frequencies for synchrotron-based x-ray microscopy *Crystals* **12** 1029
[14] Dubs C, Surzhenko O, Thomas R, Osten J, Schneider T, Lenz K, Grenzer J, Hübner R and Wendler E 2020 Low damping and microstructural perfection of sub-40nm-thin yttrium iron garnet films grown by liquid phase epitaxy *Phys. Rev. Mater.* **4** 024416
[15] Mayr S, Finizio S, Reuteler J, Stutz S, Dubs C, Weigand M, Hrabec A, Raabe J and Wintz S 2021 Xenon plasma focused ion beam milling for obtaining soft x-ray transparent samples *Crystals* **11** 546
[16] Ziegler J F, Ziegler M and Biersack J 2010 SRIM—the stopping and range of ions in matter (2010) *Nucl. Instrum. Methods Phys. Res.* B **268** 1818–23
[17] Nolle D, Weigand M, Audehm P, Goering E, Wiesemann U, Wolter C, Nolle E and Schütz G 2012 Note: unique characterization possibilities in the ultra high vacuum scanning transmission x-ray microscope (UHV-STXM) "MAXYMUS" using a rotatable permanent magnetic field up to 0.22 T *Rev. Sci. Instrum.* **83** 046112
[18] Kalinikos B A and Slavin A N 1986 Theory of dipole-exchange spin wave spectrum for ferromagnetic films with mixed exchange boundary conditions *J. Phys. C: Solid State Phys.* **19** 7013–33
[19] Klos J W and Krawczyk M 2018 Magnonic crystals: from simple models toward applications: properties and applications *Magnetic Structures of 2D and 3D Nanoparticles* (Jenny Stanford Publishing) pp 283–331
[20] Lin Y, Almasi G and Keefe G 1977 Contiguous-disk bubble domain devices *IEEE Trans. Magn.* **13** 1744–64
[21] Fodchuk I, Kotsyubynsky A, Velychkovych A, Hutsuliak I, Boychuk V, Kotsyubynsky V and Ropyak L 2022 The effect of Ne+ ion implantation on the crystal, magnetic and domain structures of yttrium iron garnet films *Crystals* **12** 1485
[22] Ostafiychuk B K, Fedoriv V D, Yaremiy I P, Garpul O Z, Kurovets V V and Yaremiy I C 2011 Implantation of single crystalline iron garnet thin films with He+, B+ and Si+ ions *Phys. Status Solidi* a **208** 2108–14